

X-ray characterization of the pulsar PSR J1849–0001 and its wind nebula G32.64+0.53 associated with TeV sources detected by H.E.S.S., HAWC, Tibet AS γ , and LHAASO

CHANHO KIM ¹, JAEGEUN PARK ¹, JOOYUN WOO ², SARAH SILVERMAN,² HONGJUN AN ¹, AYA BAMBA ^{3,4,5},
KAYA MORI ², STEPHEN P. REYNOLDS ⁶, AND SAMAR SAFI-HARB ⁷

¹*Department of Astronomy and Space Science, Chungbuk National University, Cheongju, 28644, Republic of Korea*

²*Columbia Astrophysics Laboratory, 550 West 120th Street, New York, NY 10027, USA*

³*Department of Physics, Graduate School of Science, The University of Tokyo, 7-3-1 Hongo, Bunkyo-ku, Tokyo 113-0033, Japan*

⁴*Research Center for the Early Universe, School of Science, The University of Tokyo, 7-3-1 Hongo, Bunkyo-ku, Tokyo 113-0033, Japan*

⁵*Trans-Scale Quantum Science Institute, The University of Tokyo, Tokyo 113-0033, Japan*

⁶*Physics Department, NC State University, Raleigh, NC 27695, USA*

⁷*Department of Physics and Astronomy, University of Manitoba, Winnipeg, MB R3T 2N2, Canada*

ABSTRACT

We report on the X-ray emission properties of the pulsar PSR J1849–0001 and its wind nebula (PWN), as measured by Chandra, XMM-Newton, NICER, Swift, and NuSTAR. In the X-ray data, we detected the 38-ms pulsations of the pulsar up to ~ 60 keV with high significance. Additionally, we found that the pulsar’s on-pulse spectral energy distribution displays significant curvature, peaking at ≈ 60 keV. Comparing the phase-averaged and on-pulse spectra of the pulsar, we found that the pulsar’s off-pulse emission exhibits a spectral shape that is very similar to its on-pulse emission. This characterization of the off-pulse emission enabled us to measure the >10 keV spectrum of the faint and extended PWN using NuSTAR’s off-pulse data. We measured both the X-ray spectrum and the radial profiles of the PWN’s brightness and photon index, and we combined these X-ray measurements with published TeV results. We then employed a multizone emission scenario to model the broadband data. The results of the modeling suggest that the magnetic field within the PWN is relatively low ($\approx 7\mu\text{G}$) and that electrons are accelerated to energies $\gtrsim 400$ TeV within this PWN. The electrons responsible for the TeV emission outside the X-ray PWN may propagate to ~ 30 pc from the pulsar in ~ 10 kyr.

1. INTRODUCTION

It is well known that high-energy electrons exist in pulsar wind nebulae (PWNe), as evidenced by detections of very high-energy (≥ 100 GeV) photons emitted from them. Indeed, numerous H.E.S.S. and LHAASO sources detected at energies above 10 TeV are associated with X-ray PWNe (e.g., [H. E. S. S. Collaboration et al. 2018](#); [Cao et al. 2023](#)). Theories suggest that electrons and positrons are accelerated at the termination shock (TS), which is formed by the interaction between a pulsar’s wind and the ambient medium ([Kennel & Coroniti 1984b](#)). These energetic leptons propagate outward from the TS by advection and diffusion (e.g., [de Jager & Djannati-Ataï 2009](#)), generating a bubble of synchrotron radiation, i.e., a PWN. Elec-

trons injected by old pulsars would have sufficient time to travel large distances from the pulsars, and these electrons are believed to contribute to the formation of TeV halos around aged pulsars ([Abeysekara et al. 2017](#); [H. E. S. S. Collaboration et al. 2023](#)). Additionally, PWNe may play a role in generating the high-energy cosmic-ray electrons/positrons detected on Earth (e.g., [Adriani et al. 2009](#); [Manconi et al. 2020](#)).

While young systems can accelerate electrons to very high energies ([LHAASO Collaboration et al. 2021](#)), due to radiative cooling, these electrons would not retain their energies when they escape from the compact X-ray emission region. Electrons that emit TeV photons via the inverse-Compton scattering process are expected to cool within a few kyrs if the magnetic field (B) within the PWN is strong (e.g., $B = 20\text{--}100\mu\text{G}$ in young PWNe; [Bamba et al. 2010a](#); [Torres et al. 2014](#)). Consequently, electrons generated during the early stages of PWN evolution (when B was higher) cannot account for

Corresponding author: Hongjun An
hjan@cbnu.ac.kr

the high-energy electrons responsible for creating TeV halos and the energetic cosmic-ray electrons detected on Earth. On the other hand, low- B PWNe associated with middle-aged (characteristic age τ_c of 10–100 kyr) pulsars with high spin-down power ($\dot{E}_{\text{SD}} > 10^{36}$ erg s $^{-1}$) are good candidates for producing high-energy electrons/positrons within the Galaxy.

Recent studies have provided evidence of PeV electrons within several middle-aged PWNe (e.g., LHAASO Collaboration et al. 2021; Burgess et al. 2022; Woo et al. 2023) through the modeling of their broadband spectral energy distributions (SEDs). These high-energy electrons propagate outward, and they eventually escape from the PWNe and are injected into the ISM. However, the injection rates and energetics of electrons remain unclear. These quantities depend on the flow properties and energy-loss mechanisms within PWNe (e.g., Reynolds 2016), which can be investigated by modeling spatially varying properties and broadband SEDs of PWNe (e.g., Park et al. 2023a) across different evolutionary stages. Of particular significance is investigating the most energetic electrons (> 100 TeV), which is most effectively accomplished by analyzing their synchrotron X-ray emission, while the inverse-Compton emission in TeV energies is suppressed by the Klein-Nishina effect. Therefore, studying broadband X-ray emission properties of PWNe with proper multi-zone modeling is essential, especially for those associated with energetic pulsars and TeV sources (e.g., Mori et al. 2022).

The bright X-ray source IGR J1849–0000 was discovered by INTEGRAL (Molkov et al. 2004). A follow-up XMM-Newton observation (Terrier et al. 2008) resolved the INTEGRAL source to a point source and extended emission ($\approx 150''$), suggesting a pulsar+PWN system. The pulsar hypothesis was substantiated by the detection of a 38-ms pulsation (PSR J1849–0001; J1849 hereafter; Gotthelf et al. 2011) and $\dot{P} = 1.42 \times 10^{-14}$ s s $^{-1}$. The measured P and \dot{P} values imply a surface magnetic field $B_S = 7.5 \times 10^{11}$ G, spin-down power $\dot{E}_{\text{SD}} = 9.8 \times 10^{36}$ erg s $^{-1}$, and characteristic age $\tau_c = 43$ kyr, thus categorizing the point source as an energetic and middle-aged pulsar. Furthermore, this middle-aged pulsar and its PWN are of particular interest as their emission is significantly detected above 100 TeV by HAWC (Albert et al. 2020), LHAASO (Cao et al. 2023), and Tibet air shower array (Tibet AS γ ; Amenomori et al. 2023) with the maximum photon energy of 350 TeV (Cao et al. 2021). This indicates the presence of en-

ergetic particles within the PWN (G32.64+0.53 1 ; G32.6 hereafter).

Kuiper & Hermsen (2015) conducted an in-depth analysis of Chandra, XMM-Newton, RXTE, and INTEGRAL data of the J1849+G32.6 system and found that the pulsed spectrum of the pulsar is well described by a power-law model with a hard photon index of $\Gamma = 1.37$. They further compared this ‘pulsed (on–off)’ spectrum with the total (on+off) spectrum measured with INTEGRAL, as Terrier et al. (2008) did. Based on this comparison, both of these previous studies suggested that the pulsar exhibits a curved spectrum. Additionally, Kuiper & Hermsen (2015) observed that the PWN emission in the inner region, as measured with the Chandra data, exhibits a harder spectrum compared to the spectrum from the outer region, as measured with the XMM-Newton data. They attributed this spectral change to the synchrotron burn-off effect.

Further exploration of the spatially varying PWN emission can give insights into particle transport mechanisms within the source (e.g., Tang & Chevalier 2012; Porth et al. 2016; Kim & An 2020), subsequently exploring how energetic electrons are injected into the ISM. Moreover, the spectral softening could potentially manifest as a high-energy spectral break in the spatially-integrated spectrum; NuSTAR’s hard X-ray data may facilitate detecting a spectral break (e.g., Nynka et al. 2014; Madsen et al. 2015a) or a cut-off (e.g., An 2019) at energies ≥ 10 keV. Furthermore, a precise characterization of the putative curvature in J1849’s spectrum can offer insights into the mechanism of pair production in rotation-powered pulsars (Harding & Kalapotharakos 2017).

In this paper, we carry out an X-ray characterization of the emissions from the pulsar J1849 and its wind nebula G32.6 using archival X-ray observations as well as new NuSTAR data. We present the results of our X-ray data analyses in Section 2 and construct a broadband SED of the PWN by supplementing our X-ray measurements with the TeV results of H.E.S.S., HAWC, LHAASO, and Tibet AS γ (Section 3). We employ a multi-zone emission model to interpret the broadband data and infer the properties of this PWN (Section 3). We discuss the results in Section 4 and present a summary in Section 5. The uncertainties reported in this paper correspond to 1σ confidence intervals unless otherwise noted.

2. X-RAY DATA ANALYSIS

¹ <http://snrcat.physics.umanitoba.ca/>

Table 1. Pulsar timing parameters

Parameter	Value
Range of dates (MJD)	57831–59774
Epoch (MJD TBD)	58239.91628621966
Frequency (Hz)	25.9590178608(4)
1st derivative (Hz s ⁻¹)	$-9.54076(2) \times 10^{-12}$
2nd derivative (Hz s ⁻²)	$1.74(2) \times 10^{-22}$
3rd derivative (Hz s ⁻³)	$-3.16(9) \times 10^{-30}$
4th derivative (Hz s ⁻⁴)	$3.9(2) \times 10^{-38}$

2.1. Data reduction

We analyzed the X-ray observation data of J1849 obtained by Chandra, XMM-Newton, NICER, Swift, and NuSTAR. We reprocessed the Chandra ACIS-S data acquired on 2012 Nov. 16 for 23 ks (Obs. ID 13291) using the `chandra_repro` tool of CIAO 4.14. The XMM-Newton observation (2011 Mar. 23; Obs. ID 0651930201) was carried out with the full-frame and small-window mode for the MOS and the PN detectors, respectively. We processed these data with the `emproc` and `eproc` tools of SAS 20211130_0941, and we further removed particle flares following the standard procedure. Net XMM-Newton exposures after the data screening are 47 ks, 50 ks, and 37 ks for MOS1, MOS2, and PN, respectively. The NICER data were collected between 2018 Feb. 13 and 2022 Jul. 14 (143 observations with the Obs. IDs 1020660101–5505050501). We processed the NICER observations using the `nicer12` script integrated in HEASOFT v6.31. We also used the Swift windowed-timing mode data taken on 2017 Mar. 19 for 12.5 ks (Obs. ID 00034978002) to extend the baseline for our pulsar timing study (Section 2.2). The Swift data were processed with the `xrtpipeline` tool. The source was observed by NuSTAR on 2020 Nov. 24, and we processed the data using `nupipeline` along with the `strict` SAA filter. The net exposure of the NuSTAR observation is 51 ks for each of FPMA and FPMB.

2.2. Pulsar timing analysis

A timing solution for J1849, valid between MJDs 57830.9 and 58391.0, was reported by Bogdanov et al. (2019) (see also Ho et al. 2022). We extend this solution to cover the 5.4-year period spanning the epochs of the Swift, NICER, and NuSTAR observations. In the Swift data, we extracted events within an $R = 16''$ circle centered at the pulsar in the 1–6 keV band, while for the NuSTAR data, we used an $R = 60''$ extraction circle in the 3–60 keV band. Because the source pulsations were not well detected by NICER below 2 keV, we employed the 2–8 keV band for the NICER analysis. Our analysis included 108 NICER observations (for both timing and spectral analyses) in which the pulse profiles were con-

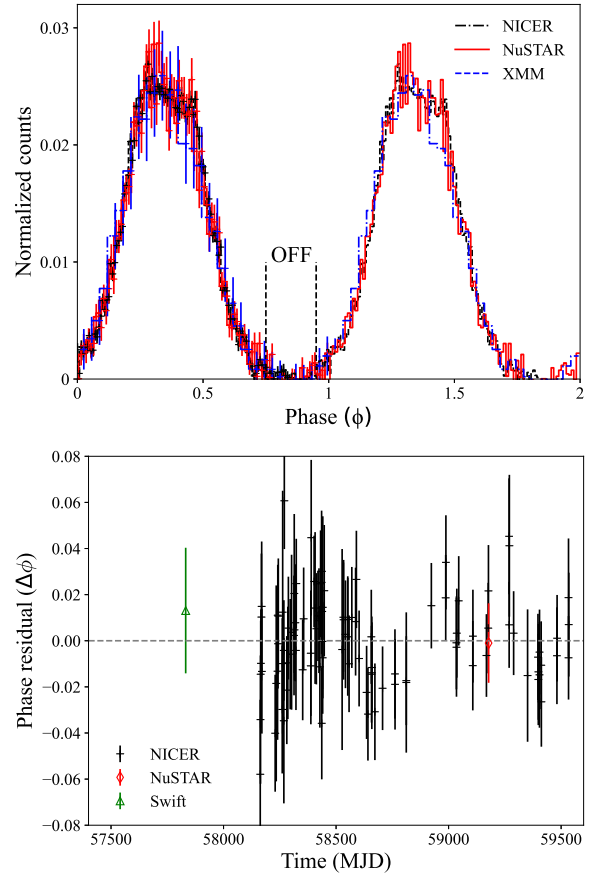


Figure 1. *Top:* Pulse profiles in the 1–10 keV (blue; XMM-Newton), 2–8 keV (black; NICER), and 3–60 keV (red; NuSTAR FPMA and FPMB combined) bands. Backgrounds and off-pulse emissions are subtracted from the profiles, and each profile is normalized to have an integrated count of 1. The vertical dashed lines denote the off-pulse interval ($\phi=0.75\text{--}0.95$). The reference phase ($\phi = 0$) of the XMM-Newton profile was adjusted to align with the NICER and NuSTAR profiles. Two cycles are shown for clarity. *Bottom:* Phase residuals after optimizing the timing solution (see text).

fidently measured. We applied barycenter corrections to the photon arrival times, utilizing the source position (R.A., decl.)=(282.2568023°, -0.0216153°), and carried out a semi-phase-coherent timing analysis (e.g., An & Archibald 2019).

We constructed a pulse-profile template using the Swift and NICER data for which the existing solution is valid (MJD 57830.9–58391.0). We then fit the template with a double-Gaussian function and used the function in our analysis. We progressively folded the later observations and measured a phase shift of each observation by fitting the observed pulse profile with the function. In the case that notable drifts occurred in the pulse-arrival phases, we updated the timing solution by introducing a higher frequency derivative to ensure phase

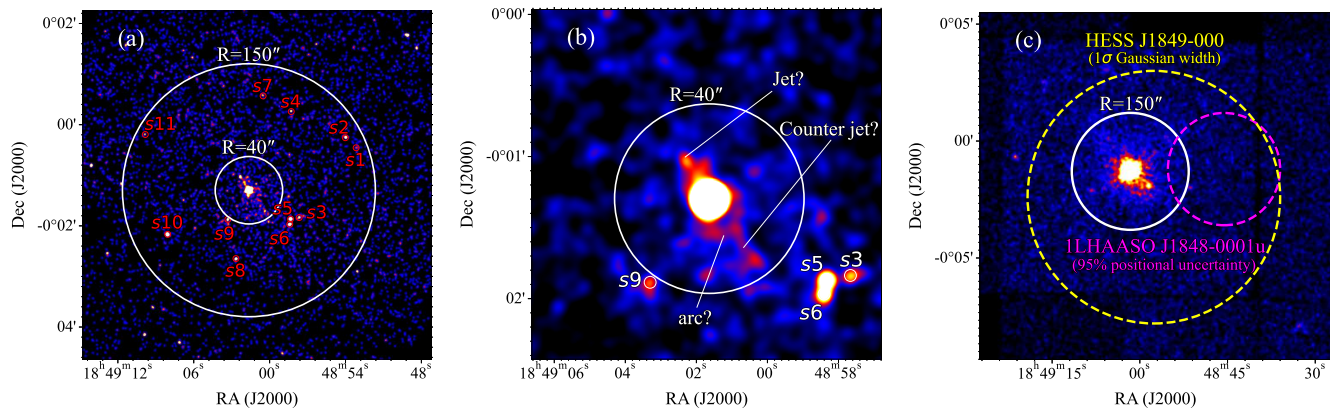


Figure 2. 1–7 keV Chandra ACIS-S (panels (a) and (b)) and XMM-Newton MOS (panel (c)) count images of the pulsar J1849 and its PWN. For legibility, the images are logarithmically scaled and smoothed with a Gaussian kernel having 1σ widths of 2.5, 4, and 1.3 pixels in panels (a), (b), and (c), respectively. (a) Red circles denote contaminating point sources within an $R = 150''$ region. A $40''$ circle is shown for reference. (b) In this zoomed-in Chandra image, a jet and counter-jet structure in the northeast-southwest direction and an arc structure are apparent, but the detection significance for these structures was low ($\leq 2.5\sigma$). (c) Faint and extended emission from the PWN is visible out to $R \lesssim 150''$. A bright spot in the southwest of the pulsar is produced by the point sources S3, S5, and S6 (see panel (a)). The H.E.S.S. source (0.09° ; 1σ Gaussian width) and the LHAASO (0.04° ; 95% positional uncertainty) source are denoted by yellow and magenta circles, respectively.

alignment. Following this, we created a new pulse-profile template using the revised timing solution and updated the Gaussian function. We repeated this procedure for all the Swift, NICER, and NuSTAR observations. To ensure phase coherence across the Swift, NuSTAR, and 4.5 yr NICER data, it was necessary to incorporate four frequency derivatives. The results of this semi-phase-coherent analysis are presented in Table 1 and Figure 1. The source pulsations were significantly detected up to the 50–60 keV band by NuSTAR with a chance probability of 6×10^{-4} .

Because our timing solution is not valid at the much earlier XMM-Newton observation epoch due to the uncertainties in the timing parameters, we performed H tests (de Jager et al. 1989) to measure the XMM-Newton pulse profile. For this analysis, we used the 1–10 keV band and an $R = 16''$ circular region to extract source events from the PN data. We conducted a search for pulsations around the previously reported period, while holding \dot{P} fixed at the measured value of 1.4224×10^{-14} (Gotthelf et al. 2011; Kuiper & Hermsen 2015). The pulsations were detected with high significance with an H statistic of ~ 4000 . The XMM-Newton-measured profile is displayed in Figure 1. The on-pulse profiles (off-pulse emission was subtracted using the phase interval $\phi=0.75$ – 0.95) measured with the three observatories agree with each other very well, and we further verified that the on+off profiles measured with XMM-Newton and NuSTAR, obtained by subtracting the background taken from circular regions ($R = 32''$ for XMM-Newton and $R = 60''$ for NuSTAR) at $R \sim 150''$ from the pulsar, also agreed well with each other. It is

important to note that the pulsations were significantly detected in the <2 keV band of the PN data. This means that the non-detection of <2 keV pulsations in the NICER data likely results from elevated background levels (e.g., flares) present in the data, rather than originating from intrinsic emission properties of J1849 or the influence of strong Galactic absorption.

2.3. Image analysis

While the extended PWN G32.6 has been previously identified (Terrier et al. 2008; Gotthelf et al. 2011; Kuiper & Hermsen 2015; Vleschower Calas et al. 2018), a careful image analysis of the Chandra, XMM-Newton, and NuSTAR data is required to assess contamination by the pulsar in the PWN emission region. This is crucial for analyzing the low imaging resolution data collected by XMM-Newton and NuSTAR. The optics vignetting effect is not a concern for our investigation of the central region (e.g., $< 30''$). At $R = 150''$, this effect was estimated to be ~ 3 – 8% for XMM-Newton and Chandra, and $\sim 14\%$ for NuSTAR.

2.3.1. Analysis of the Chandra and XMM-Newton images

We present the 2–7 keV count image measured by Chandra in panels (a) and (b) of Figure 2. The central $R \lesssim 1''$ region is significantly affected by the pile-up effect caused by the bright pulsar. The $R \lesssim 40''$ region surrounding the pulsar appears brighter than other regions and displays some possible substructures. These include a jet-like feature in the northeast direction, a counterjet in the southwest direction (distinct from the readout trail), and an arc to the south of the pulsar.

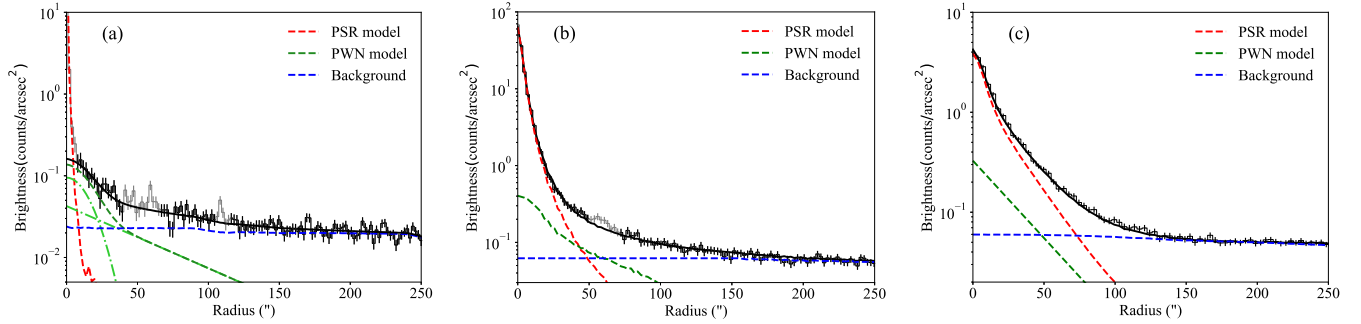


Figure 3. Radial profiles measured with Chandra and XMM-Newton/MOS in the 2–7 keV (panels (a) and (b)), as well as with NuSTAR in the 5–50 keV band (panel (c)). The red, green, and blue curves correspond to the pulsar, PWN, and background models, respectively, and the solid black curve is the summed model. In panel (a), the dot-dashed lines are the Gaussian and exponential functions used for the PWN model (see text). The gray data points in panels (a) and (b) are ignored in our fits as they are contaminated by the piled-up pulsar ((a)) or other point sources ((a) and (b)).

However, each of these structures is statistically insignificant ($\leq 2.5\sigma$).

On a larger scale, the extended PWN with a radius of $R \approx 150''$ (Figure 2 (c)) is detected by XMM-Newton, as previously reported (e.g., Terrier et al. 2008). This X-ray PWN overlaps with the regions of TeV emission measured by H.E.S.S and LHAASO (H. E. S. S. Collaboration et al. 2018; Cao et al. 2023). HAWC has also identified a source with a 0.16° offset in the north-east direction (Albert et al. 2020).

We further characterized the PWN emission using radial profiles around the pulsar position. The Chandra profile (Figure 3 (a)) exhibits J1849, a narrow core, and a broad wing. The latter two components extend to large distances, representing the extended PWN. The profile also shows spiky features that arise from contamination by point sources within the field. To model the Chandra profile, we considered a uniform background (exposure map) and a PWN model, while excluding the piled-up pulsar ($R \leq 6''$) and other contaminating sources. However, we found that a single-component model for the PWN emission failed to adequately fit the data. Consequently, we adopted a two-component function, a Gaussian combined with an exponential tail: $A\exp(-r^2/2\sigma^2) + B\exp(-r/l)$. This function successfully fit the data, as illustrated in Figure 3 (a), with the best-fit parameters of $\sigma = 10.8 \pm 2.2''$ and $l = 49.5 \pm 5.8''$.

We also carried out an analysis of the 1D radial profile derived from the XMM-Newton/MOS data (Figure 3 (b)). For the analysis of the profile, we utilized the MOS point spread functions (PSFs) generated using the `psfgen` tool of SAS to represent the pulsar emission. To construct a PWN model, we convolved the Chandra PWN model with the XMM-Newton PSFs. In this analysis, we adopted a flat background, i.e., the exposure map, and fit the profile by optimizing the normalization

factors of the PSF, PWN, and background components. In the fitting procedure, we excluded regions that were contaminated by point sources, such as the small bump at $R \approx 60''$. The results are shown in Figure 3 (b). Notably, within a radius of $R \leq 50''$, the pulsar appears brighter than the PWN, and in the central $16''$ region, the estimated 2–10 keV PWN counts amount to $<2\%$ of the pulsar’s count.

The XMM-Newton/PN small-window image, despite its limited coverage of the PWN, allowed the distinction between the on- and off-pulse emission from the pulsar. We generated radial profiles of the PN data utilizing the on- and off-pulse intervals defined in Figure 1, and then fit these profiles with the same model applied to the MOS data. Our analysis revealed that the 2–7 keV off-pulse emission from the pulsar (i.e., PSF) is $22 \pm 1\%$ of its on–off emission (per spin cycle).

2.3.2. Analysis of the NuSTAR image

The pulsar’s emission is so intense that the faint and extended PWN is not clearly visible in NuSTAR’s 2D images. So we performed an analysis of the 5–50 keV radial profile of the NuSTAR data, as displayed in Figure 3 (c). Similar to the approach used for the Chandra and XMM-Newton profiles, we fit the NuSTAR profile with the PSF, PWN function and background.

NuSTAR’s PSF (An et al. 2014b; Madsen et al. 2015b) is considerably broader compared to both the Chandra’s PSF and the Gaussian core of the PWN profile measured by Chandra. As a result, the PSF-convolved PWN function essentially appears as an exponential function. Besides, it is unclear whether the PWN profile in the 5–50 keV band is the same as the low-energy Chandra profile. In light of these complications, we opted for an exponential function instead of the PSF-convolved PWN function for modeling the NuSTAR profile. Upon analysis, the best-fit width of the exponen-

tial function was determined to be $l = 28'' \pm 3''$, which is smaller than the Chandra-derived l of $49.5'' \pm 5.8''$. This discrepancy possibly suggests a decrease in size with increasing energy, although it could also be attributed to the influence of the Gaussian core observed in the Chandra profile.

The high temporal resolution of NuSTAR enabled us to independently measure the on- and off-pulse emissions. By analyzing the radial profiles of the on- and off-pulse data, we found that the off-pulse pulsar emission within the 5–50 keV band is $22.1 \pm 1.5\%$ of the on–off emission. This estimation is consistent with the $22 \pm 1\%$ obtained from the XMM-Newton/PN profile (Section 2.3.1). Consequently, we conclude that the ratio of counts in the off- and on-pulse emission does not vary significantly in the broad X-ray band.

2.4. Spectral analysis

As previously mentioned, the prominent pulsar emission dominates over the PWN emission in the XMM-Newton and NuSTAR data. This section aims to precisely characterize the pulsar’s spectrum by using the NICER, XMM-Newton, and NuSTAR data (Section 2.4.1). This is crucial to the NuSTAR measurement of the PWN spectrum because contamination of the PWN region by the pulsar’s emission is a concern in the NuSTAR analysis. While the strong contamination from the on-pulse emission of the pulsar can be minimized by using the off-pulse interval (Figure 1) in the measurement of the PWN spectrum, there is still some contamination from the pulsar’s off-pulse emission. We characterize this off-pulse spectrum using the XMM-Newton data by comparing the “on+off” spectrum, in which contamination from the PWN is negligible, with the “on–off” spectrum, as shown below (Section 2.4.2). Additionally, we assess contamination by other point sources within the PWN (Section 2.4.3). Subsequently, we take into account emissions from the pulsar and other point sources when measuring the PWN spectra (Sections 2.4.3 and 2.4.4).

We performed spectral fitting in XSPEC v12.13.0c by employing the χ^2 statistic. To account for Galactic absorption, we adopted the `tbabs` model with the `wilm` abundances (Wilms et al. 2000) and the `vern` cross section (Verner et al. 1996).

2.4.1. On–off spectrum of the pulsar J1849

To measure the “on–off” spectrum of J1849, we selected events within the on- and off-pulse intervals (Figure 1) from the XMM-Newton/PN, NICER, and NuSTAR data. For extracting on-pulse (source) spectra, circular regions with radii of $R = 16''$ and $R = 60''$

were employed for XMM-Newton and NuSTAR, respectively. The off-pulse (background) spectra were extracted within the same regions used for the source regions. As for the NICER data, source and background spectra were extracted from each of the 108 observations. We then combined these NICER spectra using the `addascaspec` script to construct high-quality source and background spectra. Corresponding spectral response files were generated following the standard procedure suitable for each observatory. We then grouped the source spectra to ensure at least 20 counts per spectral bin.

We jointly fit the on–off spectra measured by XMM-Newton, NICER, and NuSTAR with an absorbed power-law (PL) or the log parabolic power-law (`logpar`; Massaro et al. 2004) model. For each spectrum, a cross-normalization factor was incorporated, with the factor for the NICER spectrum set to 1. The energy bands used were 0.3–10 keV, 2–8 keV, and 5–60 keV for the XMM-Newton, NICER, and NuSTAR spectra, respectively. The selection of these energy bands aimed to minimize contamination from background and (cross-) calibration uncertainties (e.g., Madsen et al. 2022).

While the PL fit was acceptable, adopting the `logpar` model resulted in an improved fit (Table 2 and Figure 4). The latter model was favored with an f -test probability of 5×10^{-5} . The cross-normalization factors for the NuSTAR spectra were consistent with 1 at $\lesssim 1\sigma$ levels. However, the factor for the XMM-Newton/PN spectrum was measured to be 0.94 ± 0.02 , exhibiting a deviation from 1 at a $\sim 3\sigma$ significance level. This discrepancy might indicate some systematic effects, potentially stemming from cross-calibration issues (see Madsen et al. 2017). These cross-normalization factors are taken into account below while measuring the PWN spectrum.

Our estimation of $N_{\text{H}} = (6.4 \pm 0.4) \times 10^{22} \text{ cm}^{-2}$ towards the source is larger than previous results of $(4.0\text{--}4.5) \times 10^{22} \text{ cm}^{-2}$ (Terrier et al. 2008; Gotthelf et al. 2011; Kuiper & Hermsen 2015; Vleschower Calas et al. 2018). We believe that the discrepancy could be ascribed to a different abundance model that these authors used. Although they did not report the abundance model, we were able to reproduce their N_{H} values by using the `angr` abundances (default in XSPEC).

2.4.2. Estimations of the off-pulse spectrum of the pulsar

Estimating the pulsar emission within the ‘off-pulse interval’ is crucial for accurately measuring the $R = 150''$ PWN spectrum using the NuSTAR data. Based on our analysis results presented so far, we considered that contamination of the PWN region by the pulsar’s off-pulse emission would not be negligible. While our

Table 2. Spectral analysis results

Data	Instrument ^a	Model ^b	Energy (keV)	N_{H} (10^{22} cm^{-2})	Γ/a	b	$F_{2-10 \text{ keV}}^c$	χ^2/dof	Comment
PSR	XP+Ni+Nu	logpar	0.3–60	6.4 ± 0.4	1.40 ± 0.03	0.38 ± 0.09	4.09 ± 0.07^d	1325/1296	on–off
PSR	XP+Ni+Nu	PL	0.3–60	8.1 ± 0.2	1.42 ± 0.03	...	4.29 ± 0.07^d	1342/1297	on–off
PSR	XM+XP	PL	0.3–10	6.7 ± 0.2	1.21 ± 0.03	...	4.75 ± 0.06	820/811	on+off
PSR	XP	PL	0.3–10	6.7^e	1.20 ± 0.04	...	3.85 ± 0.06^d	456/410	on–off
PWN	CXO	PL	0.3–10	6.4^f	$1.96 \pm 0.33 \pm 0.12^g$...	$1.44 \pm 0.18 \pm 0.02^g$	43/45	
PWN	Nu	PL	5–20	6.4^f	$2.64 \pm 0.41 \pm 0.36^g$...	$1.94 \pm 0.68 \pm 0.11^g$	56/61	
PWN	CXO+Nu	PL	0.3–20	6.4^f	$2.25 \pm 0.29 \pm 0.15^g$...	$1.37 \pm 0.15 \pm 0.05^g$	104/107	

^aXP: XMM-Newton/PN, XM: XMM-Newton/MOS, Ni: NICER, Nu: NuSTAR, CXO: Chandra.

^b $K(E/E_p)^{-a-b \log(E/E_p)}$ with $E_p = 10 \text{ keV}$ for logpar and $K(E/1 \text{ keV})^{-\Gamma}$ for PL.

^cAbsorption-corrected 2–10 keV flux in units of $10^{-12} \text{ erg s}^{-1} \text{ cm}^{-2}$.

^dSpin-cycle averaged flux.

^eFixed at the value obtained from the fit of the XM on+off spectrum.

^fFixed at the value obtained from the logpar model of the XP+Ni+Nu on–off spectra.

^gThe second error denotes the systematic uncertainty (see Section 2.4.3).

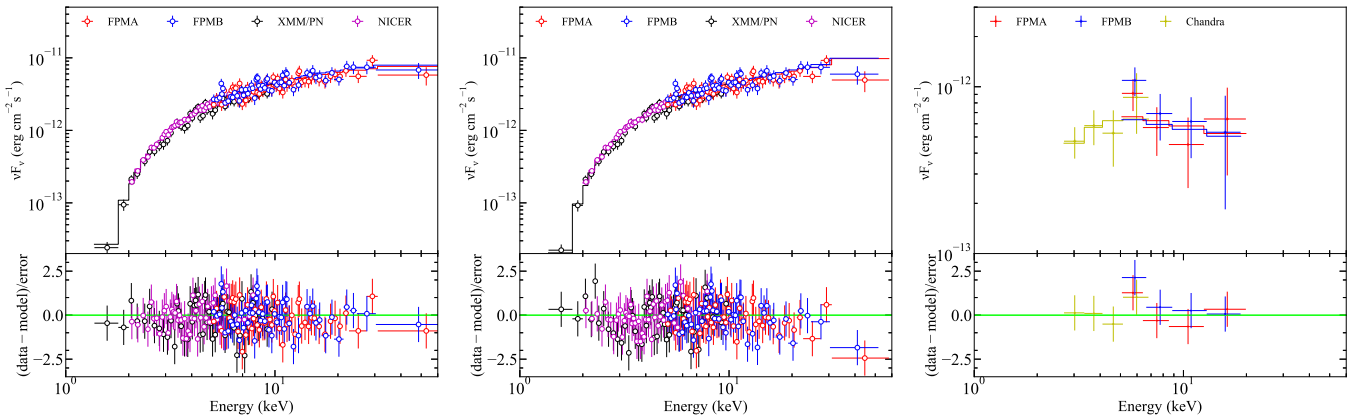


Figure 4. (Left): X-ray spectra of J1849 measured with XMM-Newton (black), NICER (purple), and NuSTAR (red and blue) and the best-fit logpar model (solid curves). The pulsar spectra were measured in the on-pulse interval by subtracting the off-pulse background (i.e., on–off) and were averaged over a spin cycle. (Middle): PL fit of the on–off spectra of J1849. (Right): The PWN spectra measured with Chandra (yellow) and NuSTAR (red and blue) and the best-fit PL model. The bottom panels show the fit residuals

image analysis already suggests that the off-pulse spectral shape is similar to that of the ‘on–off’ spectrum, XMM-Newton’s moderate angular resolution offers another means to probe the off-pulse spectral shape. By focusing on an $R = 16''$ circular region centered at the pulsar, we found that the PWN contributes less than 2% to the measured XMM-Newton on-pulse counts (Section 2.3.1). This contribution can be further reduced by adequately selecting a background region and would be so minor that we can safely assume the spectrum of the $R \leq 16''$ region accurately represents the pulsar’s emission. This assumption enables us to estimate the ‘‘off-pulse’’ spectrum through a comparison of the ‘‘on+off’’ and ‘‘on–off’’ spectra. For this comparison, we employ a simple PL model.

We analyzed the XMM-Newton (MOS and PN) data to measure the on+off spectra within $R = 16''$ circles centered at the pulsar. Background spectra were extracted from source-free regions on the same detector chips as the source regions, employing $R = 32''$ circles. We fit the spectra with a PL model, allowing for a variable cross-normalization factor for each instrument. These factors were found to be consistent with 1 at $\lesssim 1\sigma$ confidence levels. The results are presented in Table 2.

Although we have measured the ‘‘on–off’’ spectrum of the pulsar using the multi-mission data in the previous section, we fit the XMM-Newton/PN ‘‘on–off’’ spectrum with a PL model for a comparison with the ‘‘on+off’’ spectrum measured with MOS+PN. The results are presented in Table 2. The best-fit parameter values for this ‘‘on–off’’ spectrum are in complete

agreement with those derived from the “on+off” spectrum (Table 2). By comparing the on–off and on+off spectra, we find that the off-pulse flux is $\approx 23\%$ of the on–off flux, which is in accord with the finding in our image analysis (Section 2.3), where we determined that the off-pulse counts are $22 \pm 1\%$ of the “on–off” counts.

We further verified these results by fitting the on+off spectra (MOS1,2 and PN) with two PL components. The first PL component corresponds to the ‘off-pulse’ emission, while the second one describes the on–off spectrum. The parameters of the second PL component were held fixed at the values derived from the on–off spectrum measured with the XMM-Newton/PN data. The best-fit Γ for the first component is 1.22 ± 0.09 , and the absorption-corrected 2–10 keV flux ($F_{2-10\text{keV}}$) was determined to be $(9.1 \pm 0.5) \times 10^{-13} \text{ erg s}^{-1} \text{ cm}^{-2}$, which is consistent with the above results. In summary, we found out that the off-pulse flux is $\approx 22\%$ of the on–off flux and the off-pulse emission exhibits a very similar spectral shape to the on–off spectrum.

2.4.3. Spatially-integrated spectrum of the PWN G32.6

To characterize the spatially-integrated emission of the large PWN efficiently, it is necessary to reduce contamination from the pulsar through spatial or temporal selection. The XMM-Newton data do not allow for such selection; therefore, we measure the broadband X-ray spectra of the $R = 150''$ PWN using the Chandra and NuSTAR data. In this case, in-flight backgrounds may not accurately represent those in the large source region because of various effects, such as inhomogeneity in the detector background and optics vignetting. The sky (photon) background is affected by optics vignetting, whereas some background components, such as particle-induced background, are not affected by the optics. We remove the latter by subtracting the blank-sky data and measure the former using the blank-sky-subtracted in-flight spectrum taken in off-source regions for the Chandra analysis (see below). For the NuSTAR data, we use the `nuskybgd` simulations (Wik et al. 2014). More detailed explanations of these background estimation processes can be found in Park et al. (2023a).

For the Chandra data, we generated blank-sky events appropriate for the observational data using the `blanksky` script of CIAO. We extracted ACIS spectra from both the observational and blank-sky data within an annular region centered at J1849 with the inner and outer radii of $5''$ and $150''$, respectively. We minimized contamination from the point sources S1–11 (Figure 2 (a)) by excising an $R = 2''$ circular region centered at each source. We then subtracted the blank-sky spectrum from the observed spectrum to construct a source

spectrum. The same procedure (i.e., subtraction of the blank-sky data) was applied to extract background spectra from regions located away ($5'–6'$) from the source region. To further refine the analysis, we corrected the blank-sky-subtracted background spectrum for the vignetting effect by multiplying it with the ratio of the energy-dependent effective areas (i.e., ancillary response files) corresponding to the source and background regions.

We fit the source spectrum using a PL+`logpar` model, where the `logpar` model accounts for the contamination by the pulsar. To model the pulsar emission (i.e., `logpar`), we adopted point-source response files corresponding to the annular source region ($R = 5''–150''$), which took into account the reduced enclosed energy fraction of Chandra’s PSF. The parameters of the `logpar` model were set to the values obtained from the on–off spectrum (Section 2.4.1), and we introduced a normalization factor to account for the 22% off-pulse emission. These pulsar parameters were then held fixed. By optimizing N_{H} of the PWN model independently of the value for the pulsar model, we determined $N_{\text{H}} = (6.6 \pm 3.6) \times 10^{22} \text{ cm}^{-2}$, which is consistent with that for the pulsar model. Therefore, we linked N_{H} of the PL model to that of the `logpar` model. The PL+`logpar` model was acceptable, with the best-fit PL parameter values reported in Table 2.

The point sources S1–11 (Figure 2 (a)) may contaminate the NuSTAR data in the large $R = 150''$ region. We therefore measured their summed spectrum using the Chandra data. We constructed a source spectrum using $R = 2''$ circular regions centered at each source. A background spectrum was extracted within $R = 3''$ circular regions near the source regions. We then fit the spectrum with a PL model and inferred the best-fit parameters to be $N_{\text{H}} = (5.8 \pm 2.1) \times 10^{22} \text{ cm}^{-2}$, $\Gamma = 1.35 \pm 0.66$, and $F_{2-10 \text{ keV}} = (2.2 \pm 0.3) \times 10^{-13} \text{ erg s}^{-1} \text{ cm}^{-2}$. When these point sources were not excised from the Chandra data, the inferred PWN flux increased by $\approx 15\%$, but the photon index changed only by ≈ 0.03 . Their influence on the NuSTAR data could be larger since the spectrum is hard. While it is unclear whether the hard spectrum extends to $>8 \text{ keV}$, we use this PL model to account for the contamination in the NuSTAR analysis as a conservative estimate.

We extracted NuSTAR spectra of the PWN utilizing the off-pulse interval to minimize the contamination by the pulsar (pulse gating). We generated the source spectra using an $R = 150''$ circular region and estimated the background in the source region using the `nuskybgd` tool (Wik et al. 2014). We ensured that the simulated background spectrum matched the source-region spec-

trum well at >30 keV, where background emission is expected to be dominant. We fit a PL+logpar+PL model to the NuSTAR spectra. As in the case of the Chandra analysis (see above), the logpar model accounts for the off-pulse emission. For this model, we used point-source response files and adopted the logpar parameters listed in Table 2, along with an additional normalization factor suitable for the lower flux of the off-pulse emission (22%); these pulsar parameters were frozen. The second PL model was introduced to take into account the contamination from S1–11; its parameters were held fixed at the Chandra-inferred values. The best-fit parameters for the first PL model (i.e., PWN emission) are presented in Table 2. At face value, the NuSTAR spectra are softer than the Chandra spectrum, possibly indicating a spectral break. However, the difference in the best-fit Γ values is statistically insignificant. Moreover, modeling the pulsar and S1–11 may introduce systematic uncertainties (see below).

Next, we jointly fit the Chandra and NuSTAR spectra using the PL+logpar+PL model, incorporating a cross-normalization factor for each instrument. Because the contamination from the point sources was excised from the Chandra data, the flux of the second PL was set to 0 for the Chandra spectrum. We held the parameters of the second PL component (emission from S1–S11) in the NuSTAR model fixed at the Chandra-inferred values. The model adequately fit the spectra (Figure 4 right), and the best-fit parameter values are presented in Table 2. The cross-normalization factors of the two instruments agreed within the $\leq 1\sigma$ level. Additionally, we fit the spectra with a broken-PL (BPL) plus logpar and PL. The best-fit parameters of the BPL model are $\Gamma_l = 1.8 \pm 0.3$, $\Gamma_h = 3.4 \pm 0.9$, and $E_{\text{brk}} = 6 \pm 2$ keV, but the BPL and PL models are statistically indiscernible with an f -test probability of 0.2.

Since the results may vary depending on the background selection, the assumed pulsar (logpar parameters) and point-source (PL parameters for S1–S11; relevant to NuSTAR) models, we evaluated systematic uncertainties in the inferred PL parameters for the PWN emission. We performed spectral analysis using various background estimations (e.g., regions), and logpar and point-source model parameter values (within their uncertainties). We then quantified the 1σ changes of the PWN model parameters, which are presented as the additional uncertainty in Table 2.

2.4.4. Spatially-resolved spectra of the PWN

We performed a spatially-resolved spectral analysis of the Chandra data using three annular regions with sizes of $R = 5''\text{--}20''$, $20''\text{--}50''$ and $R = 50''\text{--}150''$, to

investigate possible spectral variation within the PWN. We extracted ACIS spectra from these regions, and fit them along with background spectra constructed from the blank-sky data (Section 2.4.2). We jointly fit the spectra, taking into account the contamination by the pulsar (i.e., logpar model; see Section 2.4.3). Our analysis revealed an increase in Γ with increasing distance from the pulsar (Figure 5); however, this change is statistically insignificant due to large uncertainties.

We also used the XMM-Newton/MOS data to investigate the spatial variation of the PWN spectrum. We extracted spectra from annular regions of $R = 30''\text{--}75''$ and $R = 75''\text{--}150''$, excluding contaminating sources within the regions. For background estimation, we followed the same procedure employed in the Chandra analysis (Section 2.4.3), using the quiescence particle background (qpb) data generated by `evqpb` of SAS, instead of the blank-sky data used for Chandra (see Park et al. 2023a, for more detail). We then fit the spectra with the PL+logpar model, where the logpar model accounts for the contamination from the pulsar. As in the Chandra analysis, we introduced a normalization factor to accommodate the off-pulse emission and employed point-source response functions for the logpar model. The PL+logpar model provided a satisfactory fit to the data and the best-fit parameters for the PL component are presented in Figure 5.

These XMM-Newton measurements are consistent with the Chandra results, albeit yielding a larger Γ (≈ 2.1) for the $R = 75''\text{--}150''$ region compared to previous analyses of the same region ($\Gamma=1.7\text{--}1.8$; Terrier et al. 2008; Kuiper & Hermsen 2015; Vleeschower Calas et al. 2018). Although the difference is statistically insignificant, given the substantial uncertainties, we speculate that the contamination from the pulsar emission in the previous analyses may have contributed to the discrepancy. By omitting the pulsar model from our analysis, we were able to reproduce the previous results. It is worth noting that Gotthelf et al. (2011) also considered the contamination by the pulsar and inferred $\Gamma = 2.1 \pm 0.3$ for the PWN spectrum within an $R = 30''\text{--}150''$ annular region.

We also estimated systematic uncertainties for these spatially-resolved spectra as we did in Section 2.4.3. The systematic uncertainties were added to the statistical ones in quadrature, and Figure 5 displays the summed uncertainties.

3. MODELING THE PWN EMISSION

We constructed a broadband SED of the PWN from X-rays to TeV energies, by supplementing our X-ray measurements with published TeV

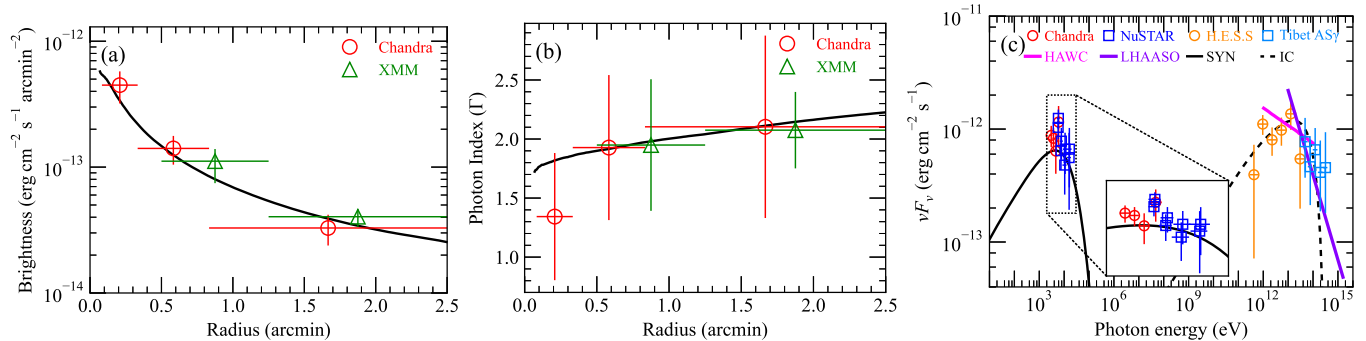


Figure 5. Radial profiles of the 2–10 keV brightness and Γ , and a broadband SED of G32.6. (a–b) Red and green points denote Chandra and XMM-Newton measurements, while black curves represent radial profiles computed by our model. (c) Red and blue points are X-ray measurements obtained from Chandra and NuSTAR, respectively. The empty orange circles in the TeV band correspond to H.E.S.S. measurements taken from H. E. S. S. Collaboration et al. (2018), and the cyan squares display Tibet AS γ measurements (Amenomori et al. 2023). Straight lines in the TeV band represent the best-fit PL models inferred from the HAWC (pink; HAWC et al. 2022) and LHAASO (purple; Cao et al. 2023) data. Our model computations for the synchrotron (SYN) and inverse-Compton (IC) emissions are presented in black solid and dashed curves, respectively.

data (H. E. S. S. Collaboration et al. 2018; Albert et al. 2020; Cao et al. 2023). The resulting broadband SED is presented in Figure 5 (c). Our X-ray characterization of the PWN emission has improved upon previous studies (e.g., Terrier et al. 2008; Gotthelf et al. 2011; Kuiper & Hermsen 2015; Vleschow Calas et al. 2018), as we included the >10 keV NuSTAR data and carefully accounted for contamination from the pulsar and S1–S11. We employed the multizone PWN model developed by Kim et al. (2019) to fit the SED as well as radial profiles of the X-ray brightness and Γ .

3.1. Description of the multizone model

Since our multizone PWN model is extensively described in Park et al. (2023a), we provide a concise overview hereafter. We assume that the pulsar injects electrons with a power-law distribution

$$\frac{dN_e}{d\gamma_e dt} = \dot{N}_0 \gamma_e^{-p_1} \quad (1)$$

between $\gamma_{e,\min}$ and $\gamma_{e,\max}$ into the TS at a distance of R_{TS} from the pulsar such that the particle energy corresponds to a fraction η_e of the pulsar’s spin-down power. The remaining power is contained in B (fraction of η_B) or radiated as gamma-ray emission from the pulsar (fraction of η_γ). As the magnetic energy is thought to be almost fully dissipated at the shock (Kennel & Coroniti 1984b), we assume $\eta_B \ll 1$ in the PWN. Additionally, the pulsar (J1849) was not detected by the Fermi Large Area Telescope (LAT; Atwood et al. 2009), indicating $\eta_\gamma \ll 1$. Therefore, in the following study, we assume $\eta_e \approx 1$. These parameters affect the energy of the electrons injected by the pulsar into the PWN, and thus the predicted flux of the PWN could vary depending on the assumed η_e . A smaller value of η_e (i.e., larger η_γ)

would cause the model to underpredict the measured fluxes (but see Section 3.3).

The electrons propagate within the PWN via advection and diffusion, and they lose energy due to radiation (synchrotron and inverse-Compton) and adiabatic expansion. Regarding the bulk flow (V_{flow}) of the electrons and B within the PWN, we adopt a power-law dependence on the distance (r) between the pulsar and an emission zone:

$$V_{\text{flow}}(r) = V_0 \left(\frac{r}{R_{\text{TS}}} \right)^{\alpha_V} \quad (2)$$

and

$$B(r) = B_0 \left(\frac{r}{R_{\text{TS}}} \right)^{\alpha_B}, \quad (3)$$

where we assume $\alpha_B + \alpha_V = -1$, which holds if the B structure is toroidal and the magnetic flux is conserved (e.g., Reynolds 2009). We assume the diffusion coefficient to be (e.g., Abeysekara et al. 2017)

$$D = D_0 \left(\frac{B}{100 \mu\text{G}} \right)^{-1} \left(\frac{\gamma_e}{10^9} \right)^{1/3}. \quad (4)$$

We let the injected electrons propagate over an assumed age of the PWN, and then we project their radiation onto the tangent plane of the observer to compute both spatially-resolved and integrated SEDs.

3.2. Basic model parameters

While the model employs multiple parameters, some of them can be estimated first based on the SED measurements and one-zone model calculations. These estimations serve as inputs for the detailed modeling (Section 3.3) and help with obtaining converged solutions more quickly.

The similar values of νF_ν for the X-ray (synchrotron) and TeV (gamma-ray) emission indicate that the magnetic energy density ($U_B \equiv \frac{B^2}{8\pi}$) is comparable to the energy density of the CMB (u_{CMB}) seed photons for inverse-Compton (IC) upscattering. From this, we estimated $B \sim 3\mu\text{G}$. Other complications, such as the contribution of the Galactic IR field and spatially varying B , are considered by the multizone model. Additionally, the measured TeV-to-X-ray flux ratio can provide information on the true age of the PWN. According to the correlations reported by [Zhu et al. \(2018\)](#), the flux ratio of ~ 1 for G32.6 suggests that its true age is 4–9 kyr, much smaller than the spin-down age ($\tau_c = 43$ kyr) of J1849. We assume t_{age} of 9 kyr in this work, but models with different values of t_{age} (and other covarying parameters, e.g., D_0) can also fit the data well (see [Park et al. 2023a](#), for parameter covariance).

Given the estimated B strength ($B \approx 3\mu\text{G}$), the synchrotron emission at ~ 20 keV detected by NuSTAR suggests $\gamma_{e,\text{max}}$ of $\geq 6 \times 10^8$. The X-ray photon index of $\Gamma \approx 1.5$ in the innermost region corresponds to the power-law index of the uncooled particle distribution of $p_1 = 2\Gamma - 1 \approx 2$. These estimations of $\gamma_{e,\text{max}}$ and p_1 allow for the determination of $\gamma_{e,\text{min}}$ since $\eta_e \approx 1$.

Although the TS of G32.6 has not been resolved likely due to its compact size obscured by the bright pulsar emission, we assumed $R_{\text{TS}} = 0.1$ pc as has been measured for several PNWe (e.g., [Ng & Romani 2004](#); [Kargaltsev & Pavlov 2008](#)). This assumption is also in accord with the correlation reported by [Bamba et al. \(2010b\)](#). Note that the exact value of R_{TS} does not significantly impact the model outputs as long as it is sufficiently smaller than the PWN size. Although the X-ray PWN does not exhibit a sharp boundary, we assumed an X-ray PWN size of $R_{\text{PWN}} = 150''$; this radial position is where we halt the advection flow and lower B to a slightly smaller value ($2.3\mu\text{G}$ in the PWN to $2\mu\text{G}$ outside). When $r > 150''$ (outside the X-ray PWN region), we do not invoke $\alpha_B + \alpha_V = -1$; both B and V_{flow} are assumed to be constant. The large region for the TeV emission ($R = 0.09^\circ$) corresponds to 11 pc for an assumed distance of 7 kpc ([H. E. S. S. Collaboration et al. 2018](#)) and implies that the TeV-emitting electrons ($\gamma_e \approx 10^7$) can go beyond the X-ray PWN due to diffusion. Considering the diffusion only, $2\sqrt{Dt_{\text{age}}} \gtrsim 10$ pc gives an estimate of $D_0 \gtrsim 1 \times 10^{26} \text{ cm}^2 \text{ s}^{-1}$ for the assumed age of $t_{\text{age}} = 9$ kyr (e.g., see [Tang & Chevalier 2012](#); [Porth et al. 2016](#); [Guest et al. 2019](#), for values of diffusion coefficients for various PNWe).

3.3. Results of modeling

We used the aforementioned estimations of the parameters (Section 3.2) as initial values for our multizone model and further adjusted them to fit the measured emission properties of G32.6. For the seeds of the IC emission, we adopted the interstellar radiation field (ISRF) estimated by GALPROP ([Porter et al. 2022](#)), along with the CMB radiation. The results are presented in Figure 5 and Table 3. Our model broadly matches the broadband SED, as well as the radial profiles of brightness and Γ .

The amplitude of the model-predicted SED is determined by a complex interplay between the spectrum of the injected electrons (e.g., η_e and p_1), the time the electrons spend in the emission region (e.g., t_{age} and V_{flow}), and the environmental factors (B and external IR seed density u_{IR}). In this work, we assumed a large value of η_e , indicating weak gamma-ray emission from the pulsar, since J1849 was not detected by the LAT. We verified that different values of η_e could be easily accommodated in our model by adjusting other parameters such as t_{age} , B , u_{IR} , and/or p_1 (see [Park et al. 2023a](#), for the parameter covariance).

An electron injection spectrum with $p_1 \approx 2$ was necessary to match the X-ray SED as well as the < 10 TeV data. For this p_1 value, a $\Gamma = 1.5$ PL emission from uncooled electrons is expected. These uncooled electrons are responsible for the $\Gamma \approx 1.5$ X-ray spectrum in the inner $R \lesssim 20''$ region. On the other hand, the $\Gamma \approx 2$ spectra in the outer regions are produced by cooled electrons. This implies that the cooling break (i.e., the peak of the curved SED) should be visible in the spatially-integrated X-ray SED. The computed SED model predicts a peak at 5 keV. Hence, the model predicts that the < 5 keV SED exhibits a harder spectrum than above the energy, as indicated by the separate fits of the Chandra and NuSTAR data; however, the broadband SED fits well with a single PL probably because of the large measurement uncertainties.

In this model, TeV emission is primarily produced by IC scattering of electrons with $\gamma_e \approx 10^7$ – 10^8 off of the CMB photons. Given the inferred B value, the assumed t_{age} of 9 kyr corresponds to the synchrotron+IC cooling timescale of $\gamma_e \sim 8 \times 10^7$ electrons. Consequently, a spectral break of the IC SED is expected at ~ 40 TeV. Moreover, the Klein-Nishina effect becomes significant for ≥ 20 TeV (IR seeds) and ≥ 100 TeV (CMB seeds) gamma rays. These factors explain the steep LHAASO SED at $\gtrsim 10$ TeV.

The radial profiles of brightness and Γ provide constraints on α_B (and thus $\alpha_V = -1 - \alpha_B$) and D_0 values. We used a slowly varying B , but different sets of α_B and D_0 can also reproduce the profiles. For the mea-

Table 3. Parameters for the SED model in Figure 5

Parameter	Symbol	Value
Spin-down power	L_{SD}	$9.8 \times 10^{36} \text{ erg s}^{-1}$
Characteristic age of the pulsar	τ_c	43 kyr
Age of the PWN	t_{age}	9000 yr
Size of the PWN	R_{pwn}	5 pc
Radius of termination shock	R_{TS}	0.1 pc
Distance to the PWN	d	7.0 kpc
Index for the particle distribution	p_1	2.12
Minimum Lorentz factor	$\gamma_{e,min}$	10
Maximum Lorentz factor	$\gamma_{e,max}$	$10^{8.9}$
Magnetic field	B_0	$7.5 \mu\text{G}$
Magnetic index	α_B	-0.3
Flow speed	V_0	$0.04c$
Speed index	α_V	-0.7
Diffusion coefficient	D_0	$1.0 \times 10^{26} \text{ cm}^2 \text{ s}^{-1}$
Energy fraction injected into particles	η_e	0.95
Energy fraction injected into B field	η_B	0.004

sured radial profiles and the assumed power-law trend for V_{flow} (Equation (2)), our model constrains α_V to be between -0.8 and -0.6 . However, it is important to emphasize that the choice of a power law for V_{flow} was made on a phenomenological basis and lacks a physical motivation and that the actual functional form of the flow in PWNe is not well-known. Our model has the flexibility to accommodate various trends; e.g., the radial profiles of V_{flow} and B predicted for ideal magnetohydrodynamic flow by Kennel & Coroniti (1984a) (see also Reynolds 2003) can also fit the data when we freely adjust the other parameters (e.g., V_0 , B_0 and D_0). These parameter values cannot be determined uniquely because of the covariance between them. The degeneracy can be broken to a certain extent if we can constrain some of the parameters; e.g., measuring the expansion speed of the PWN can help determine V_0 and α_V (Equation (2)), and B_0 can be well constrained if $u_{\text{CMB}} + u_{\text{IR}}$ are known. Nonetheless, the values presented in Table 3, which are similar to values inferred for other PWNe (e.g., Park et al. 2023b), can account for the measurements.

4. DISCUSSION

We conducted a detailed X-ray analysis of both the pulsar and PWN of the J1849+G32.6 system. We found out that the on–off emission of the pulsar exhibits a curved spectrum and the off-pulse emission has a similar spectral shape to the on–off one. By carefully accounting for the contamination from the pulsar’s emission in the low-imaging resolution XMM-Newton and NuSTAR data, we were able to characterize the PWN emission up to ~ 20 keV. The PWN emission was modeled with a simple PL having $\Gamma \approx 2$. Our results from a spatially-resolved analysis are consistent with the previously sug-

gested spectral softening in G32.6 (Kuiper & Hermsen 2015), and we measured the radial profiles of Γ and brightness. Combining our X-ray measurements with TeV SEDs, we modeled the broadband data using a multi-zone emission model for PWNe.

4.1. The Pulsar J1849

A curvature in the on–off spectrum of J1849 has been suggested by Terrier et al. (2008) and Kuiper & Hermsen (2015) based on comparisons of a low-energy on–off spectrum and a high-energy on+off spectrum. While these comparisons hinted at the presence of curvature, the definite establishment was hindered as the comparisons involved distinct quantities, on–off vs. on+off emissions. Furthermore, issues such as contamination from the PWN in the INTEGRAL data and cross-calibration problems were not addressed in the previous studies. By combining the high-quality X-ray data acquired by XMM-Newton, NICER, and NuSTAR, we were able to conclusively demonstrate the evidence of a spectral curvature in the on–off pulse emission of J1849.

The pulsar J1849 is among the four ‘MeV pulsars’ listed in Harding & Kalapotharakos (2017) (see Kuiper & Hermsen 2015, for more sources). These pulsars are young and energetic rotation-powered pulsars (RPPs) that exhibit strong emission of pulsed non-thermal X-rays while lacking significant radio or GeV emission. Harding & Kalapotharakos (2017) proposed that accurately characterizing the SEDs of MeV pulsars can aid in understanding the mechanism of pair production in RPPs. According to their study, the frequency of the SED peak (E_{SR}) of the pulsar emission is predicted to be $\propto B_S B_{\text{LC}}$, where B_{LC} represents B at the light cylinder, if the pairs are generated by polar-cap cascades. On the other hand, if the pairs are produced in the outer gap, $E_{\text{SR}} \propto B_{\text{LC}}^{7/2}$ is expected (Harding & Kalapotharakos 2017; Zhang & Cheng 2000).

Measurements of the SED peaks for PSR B1509–58 ($E_{\text{SR}} = 2.6 \pm 0.4$ MeV; Chen et al. 2016) and PSR J1846–0257 ($E_{\text{SR}} = 3.5 \pm 1.1$ MeV; Kuiper et al. 2018) indicate that the outer-gap scenario is improbable. This is evident as these two pulsars possess substantially different B_{LC} values, yet their E_{SR} values are very similar (Figure 6 top). However, testing the polar-cap scenario with these two pulsars is challenging since their $B_S B_{\text{LC}}$ values are almost the same (Figure 6 bottom).

The NuSTAR data of J1849 enabled us to measure $E_{\text{SR}} = 58_{-17}^{+43}$ keV for its SED, thereby confirming the $E_{\text{SR}}-B_S B_{\text{LC}}$ correlation (Figure 6 bottom). The inclusion of the J1849 measurement in the $E_{\text{SR}}-B_{\text{LC}}^{7/2}$ trend

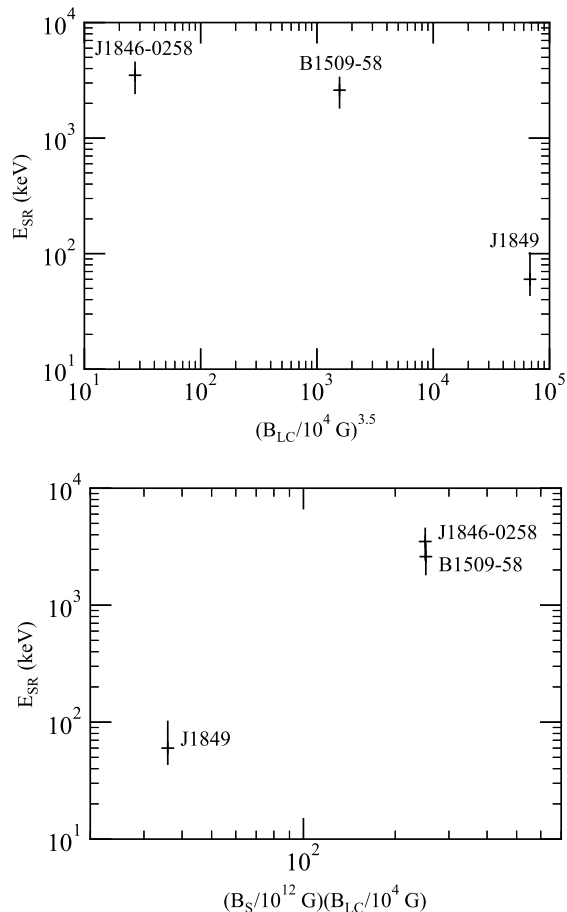


Figure 6. Measured SED peak frequencies (E_{SR}) of the synchrotron emission from three MeV pulsars versus B at the light cylinder (B_{LC} ; top) or a combination of B_s and B_{LC} (bottom).

argues against the outer-gap scenario. Measuring E_{SR} for more MeV pulsars would greatly contribute to a more detailed understanding of the pair-production mechanism.

4.2. X-ray spectra of G32.6

G32.6 displays a spectrally hard X-ray emission ($\Gamma \approx 1.5$) in the inner region ($R < 20''$ from the pulsar). We note that Kuiper & Hermsen (2015) reported smaller values of Γ in inner regions. We speculate that the discrepancy in the Γ measurements, albeit within the uncertainties, is caused by the contamination from the pulsar emission in the analysis of Kuiper & Hermsen (2015). The $\Gamma \approx 1.5$ spectrum indicates that the energy index of the electron distribution is $p_1 \approx 2$, although the large uncertainty of $\Delta\Gamma \approx 0.5$ in this region poses challenges in accurately constraining p_1 . Spatially-integrated SEDs can also offer an alternative method for determining p_1 of the uncooled electron distribution, as it is reflected in the synchrotron SED in the IR-to-

optical band or in the IC SED at energies $\lesssim 10$ TeV. However, measurements in these bands are either lacking or of poor quality, hampering precise estimations of p_1 . Moreover, the observed SED is a superposition of multi-zone emission components from various radial regions projected onto the observer’s tangent plane. Thus, the intrinsic spectrum in the inner region might have a lower value of p_1 . Nevertheless, if the inferred value of $p_1 \approx 2$ is indeed accurate, it may suggest that magnetic reconnection or shock drift acceleration plays a role in particle acceleration at the TS of PWNe (e.g., Summerlin & Baring 2012; Sironi & Cerutti 2017).

Alternatively, the $\Gamma \approx 1.5$ spectrum in the innermost region could be attributed to putative substructures such as the jet and counterjet (Figure 2 (b)), as these features can exhibit spectrally hard emission (e.g., Safi-Harb & Kumar 2008; An et al. 2014a). These substructures might potentially contain a distinct electron population. A deeper Chandra observation will facilitate more definitive detections and spectral characterization of these substructures, elucidating the origin of their hard spectra. This will, in turn, provide valuable clues about the mechanisms responsible for particle acceleration at TS of middle-aged PWNe.

At large distances from the pulsar (e.g., $R > 20''$), the X-ray spectrum follows a $\Gamma \approx 2$ PL, similar to other PWNe. In comparison to the $\Gamma \approx 1.5$ spectrum in the inner region, this indicates rapid particle cooling. As electrons travel outward within the inner region ($R \approx 20''$), they progressively lose kinetic energies. As a result, the emission peak of the highest-energy electrons will appear in the X-ray band and enable determining the flow speed and B in the PWN. However, the spectral variation over the PWN was not measured with high significance with the current X-ray data, and further confirmation of this spectral softening is necessary with future observations.

4.3. SED modeling

We applied a multizone PWN model to infer the properties of the PWN G32.6 (Table 3). While our model broadly reproduces the measurements (Figure 5), the rapid change in Γ in the inner regions, if real, is not very well explained. At face value, the $\Delta\Gamma \approx 0.5$ can be explained by synchrotron cooling, which causes a change of the spectral slope of 1 (in ideal cases) between the distributions of the injected and cooled electrons. However, the ‘observed’ spectrum is a superposition of emissions from many different radial regions, and thus the ‘observed’ difference in Γ would be diluted if observed by the current X-ray telescopes, and appear smaller than the emitted one (the inner vs. outer radial zones). This implies that the difference in the slopes of the elec-

tron distributions (relevant to the X-ray band) between $R \lesssim 20''$ (injected) and $R \gtrsim 20''$ (cooled) needs to be greater than 1. This is difficult to reproduce within the model unless we employ a broken power-law distribution for the injected electrons (such broken power laws may be required to explain large amounts of spectral steepening seen in several PWNe; [Chevalier 2005](#)).

The parameter values in Table 3 are not well constrained nor uniquely determined, as the parameters are interdependent (e.g., see [Park et al. 2023a](#)) and the quality of the measurements is rather poor; e.g., various values of η_e can reproduce the observed results, as mentioned in Section 3.3. However, if the energy densities of the seed photons estimated with the GALPROP model, despite its low angular resolution, are accurate, B_0 can be determined relatively well independently of the other parameters, based on the shapes and amplitudes of the synchrotron and IC SEDs (Section 3.3). This, in turn, helps estimate $\gamma_{e,\max}$ in combination with the NuSTAR spectrum. Moreover, the estimation of B_0 along with our measurements of the brightness and Γ profiles can help pin down α_V and V_0 if the PWN expansion rate is measured.

By fitting the radial profiles of the X-ray brightness and Γ , we inferred the index of the bulk-flow speed to be $\alpha_V = -0.7$. With this speed profile, electrons can be transported to 8.5 pc, which is sufficient to explain the observed X-ray emission zone with a size of 5 pc. The softening of the X-ray spectrum with increasing distance from the pulsar requires diffusion, as pure advection models predict a constant Γ profile in the inner regions and a rapid increase in the outer regions ([Reynolds 2003](#)). In our model, we used the diffusion coefficient of $D_0 = 10^{26} \text{ cm}^2 \text{ s}^{-1}$. In this case, electrons responsible for the TeV emission (e.g., off of IR seeds), with $\gamma_e \approx 10^7$, can move out to a distance of ~ 10 pc through diffusion and advection, which can explain the TeV emission size of 0.09° . In this region located outside the X-ray PWN, the electrons will cool primarily through IC emission and propagate further outward by diffusion. Assuming a spatially uniform ISRF with $u_{\text{IR}} = 0.5 \text{ eV cm}^{-3}$ and the ISM B (B_{ISM}) of $1 \mu\text{G}$, the cooling timescale of electrons with $\gamma_e \approx 10^7$ is estimated to be 12 kyr. Then, our model predicts that the TeV-emitting electrons will reach a distance of ~ 30 pc from the pulsar in 12 kyr and form an extensive TeV halo based on the assumed diffusion law (Equation (4)). However, this estimate is subject to substantial uncertainty since the values of u_{IR} and/or B_{ISM} may differ significantly.

Our estimate of $\gamma_{e,\max}$ corresponds to a maximum electron energy of $E_{e,\max} \approx 400 \text{ TeV}$ which is compara-

ble to 740 TeV inferred from modeling the TeV emission of G32.6 ([Amenomori et al. 2023](#)). With the lack of measurements at $>20 \text{ keV}$, our estimation of $E_{e,\max}$ should be regarded as a lower limit. Additionally, if the $\Gamma \approx 1.5$ spectrum in the innermost region represents the intrinsic spectrum of the PWN rather than putative substructures, our model predicts a spectral curvature at $\sim 5 \text{ keV}$.

5. SUMMARY

Here is a summary of our work.

- We measured the on–off spectrum of J1849 and found that its spectrum exhibits curvature with a peak at 60 keV, which supports the scenario that energetic electron-positron pairs in pulsar magnetosphere are generated by polar-cap cascades ([Harding & Kalapotharakos 2017](#)).
- The off-pulse emission of J1849 has a very similar spectral shape to the on–off one and contains $\sim 20\%$ flux of the ‘on–off’ pulse emission. This characterization allowed us to measure the broadband X-ray spectrum of the PWN.
- Our multizone emission modeling found that G32.6 can accelerate electrons to $\gtrsim 400 \text{ TeV}$. Additionally, the model predicts that the TeV emitting electrons may propagate out to a distance of ~ 30 pc from the pulsar in ~ 10 kyr, although these values may substantially alter depending on the properties (B_{ISM} and u_{IR}) of the ISM.

While we were able to accurately measure the emission properties of J1849, characterizing the PWN emission was challenging due to its faintness and strong contamination from the pulsar. Consequently, inferring the PWN properties using the model was difficult. More sensitive X-ray data, to be collected by future X-ray observatories with high angular resolution and large collecting area (e.g., AXIS and HEX-P; [Mushotzky et al. 2019](#); [Madsen et al. 2019](#)), would be highly beneficial. Additionally, further theoretical studies that encompass not only the spatial variations but also the temporal variations of PWN properties (such as flow speed, B , etc; [Gelfand et al. 2009](#); [Bandiera et al. 2023](#)) will be crucial for understanding high-energy electrons within the Galaxy.

Facilities: CXO, XMM-Newton, NICER, Swift, NuSTAR

Software: HEASoft (v6.31; NASA High Energy Astrophysics Science Analysis Center 2014), CIAO (v4.14; Fruscione et al. 2006), XMM-SAS (20211130_0941; Gabriel 2017), XSPEC (v12.12; Arnaud 1996)

1 This work used data from the NuSTAR mission, a
 2 project led by the California Institute of Technology,
 3 managed by the Jet Propulsion Laboratory, and funded
 4 by NASA. We made use of the NuSTAR Data Anal-
 5 ysis Software (NuSTARDAS) jointly developed by the
 6 ASI Science Data Center (ASDC, Italy) and the Cal-
 7 ifornia Institute of Technology (USA). JP acknowl-
 8 edges support from Basic Science Research Program
 9 through the National Research Foundation of Korea
 10 (NRF) funded by the Ministry of Education (RS-2023-
 11 00274559). AB acknowledges support from Japan
 12 Society for the Promotion of Science Grants-in-Aid
 13 for Scientific Research (KAKENHI) Grant Numbers
 14 JP23H01211. Support for this work was partially pro-
 15 vided by NASA through NuSTAR Cycle 6 Guest Ob-
 16 server Program grant NNH19ZDA001N. This research
 17 was supported by the National Research Foundation of
 18 Korea (NRF) grant funded by the Korean Government
 19 (MSIT) (NRF-2023R1A2C1002718). We thank the ref-
 20 erree for comments that helped improve the clarity of the
 21 paper.

REFERENCES

- Abeyssekara, A. U., Albert, A., Alfaro, R., et al. 2017, *Science*, 358, 911
- Adriani, O., Barbarino, G. C., Bazilevskaya, G. A., et al. 2009, *Nature*, 458, 607
- Albert, A., Alfaro, R., Alvarez, C., et al. 2020, *ApJ*, 905, 76
- Amenomori, M., Asano, S., Bao, Y. W., et al. 2023, arXiv e-prints, arXiv:2308.13781
- An, H. 2019, *ApJ*, 876, 150
- An, H., & Archibald, R. 2019, *ApJL*, 877, L10
- An, H., Madsen, K. K., Reynolds, S. P., et al. 2014a, *ApJ*, 793, 90
- An, H., Madsen, K. K., Westergaard, N. J., et al. 2014b, in *Proc. SPIE*, Vol. 9144, *Space Telescopes and Instrumentation 2014: Ultraviolet to Gamma Ray*, 91441Q
- Arnaud, K. A. 1996, in *Astronomical Society of the Pacific Conference Series*, Vol. 101, *Astronomical Data Analysis Software and Systems V*, ed. G. H. Jacoby & J. Barnes, 17
- Atwood, W. B., Abdo, A. A., Ackermann, M., et al. 2009, *ApJ*, 697, 1071
- Bamba, A., Anada, T., Dotani, T., et al. 2010a, *ApJL*, 719, L116
- . 2010b, *ApJL*, 719, L116
- Bandiera, R., Bucciantini, N., Martín, J., Olmi, B., & Torres, D. F. 2023, *MNRAS*, 520, 2451
- Bogdanov, S., Ho, W. C. G., Enoto, T., et al. 2019, *ApJ*, 877, 69
- Burgess, D. A., Mori, K., Gelfand, J. D., et al. 2022, *ApJ*, 930, 148
- Cao, Z., Aharonian, F. A., An, Q., et al. 2021, *Nature*, 594, 33
- Cao, Z., Aharonian, F., An, Q., et al. 2023, arXiv e-prints, arXiv:2305.17030
- Chen, G., An, H., Kaspi, V. M., et al. 2016, *ApJ*, 817, 93
- Chevalier, R. A. 2005, *ApJ*, 619, 839
- de Jager, O. C., & Djannati-Ataï, A. 2009, in *Astrophysics and Space Science Library*, Vol. 357, *Astrophysics and Space Science Library*, ed. W. Becker, 451
- de Jager, O. C., Raubenheimer, B. C., & Swanepoel, J. W. H. 1989, *A&A*, 221, 180
- Fruscione, A., McDowell, J. C., Allen, G. E., et al. 2006, in *Proc. SPIE*, Vol. 6270, *Society of Photo-Optical Instrumentation Engineers (SPIE) Conference Series*, 62701V
- Gabriel, C. 2017, in *The X-ray Universe 2017*, 84
- Gelfand, J. D., Slane, P. O., & Zhang, W. 2009, *ApJ*, 703, 2051
- Gotthelf, E. V., Halpern, J. P., Terrier, R., & Mattana, F. 2011, *ApJL*, 729, L16
- Guest, B. T., Safi-Harb, S., & Tang, X. 2019, *MNRAS*, 482, 1031

- H. E. S. S. Collaboration, Abdalla, H., Abramowski, A., & Aharonian, e. a. 2018, *A&A*, 612, A1
- H. E. S. S. Collaboration, Aharonian, F., Ait Benkhali, F., et al. 2023, *A&A*, 673, A148
- Harding, A. K., & Kalapotharakos, C. 2017, in *Proceedings of the 7th International Fermi Symposium*, 6
- HAWC, Abeysekara, A. U., Albert, A., et al. 2022, in *37th International Cosmic Ray Conference*, 827
- Ho, W. C. G., Kuiper, L., Espinoza, C. M., et al. 2022, *ApJ*, 939, 7
- Kargaltsev, O., & Pavlov, G. G. 2008, in *American Institute of Physics Conference Series*, Vol. 983, *40 Years of Pulsars: Millisecond Pulsars, Magnetars and More*, ed. C. Bassa, Z. Wang, A. Cumming, & V. M. Kaspi, 171–185
- Kennel, C. F., & Coroniti, F. V. 1984a, *ApJ*, 283, 694
- . 1984b, *ApJ*, 283, 710
- Kim, S., & An, H. 2020, *Astronomische Nachrichten*, 341, 170
- Kim, S., Park, J., & An, H. 2019, *Journal of Korean Astronomical Society*, 52, 173
- Kuiper, L., & Hermsen, W. 2015, *MNRAS*, 449, 3827
- Kuiper, L., Hermsen, W., & Dekker, A. 2018, *MNRAS*, 475, 1238
- LHAASO Collaboration, Cao, Z., Aharonian, F., et al. 2021, *Science*, 373, 425
- Madsen, K., Hickox, R., Bachetti, M., et al. 2019, in *Bulletin of the American Astronomical Society*, Vol. 51, 166
- Madsen, K. K., Beardmore, A. P., Forster, K., et al. 2017, *AJ*, 153, 2
- Madsen, K. K., Forster, K., Grefenstette, B., Harrison, F. A., & Miyasaka, H. 2022, *Journal of Astronomical Telescopes, Instruments, and Systems*, 8, 034003
- Madsen, K. K., Reynolds, S., Harrison, F., et al. 2015a, *ApJ*, 801, 66
- Madsen, K. K., Harrison, F. A., Markwardt, C. B., et al. 2015b, *ApJS*, 220, 8
- Manconi, S., Di Mauro, M., & Donato, F. 2020, *PhRvD*, 102, 023015
- Massaro, E., Perri, M., Giommi, P., & Nesci, R. 2004, *A&A*, 413, 489
- Molkov, S. V., Cherepashchuk, A. M., Lutovinov, A. A., et al. 2004, *Astronomy Letters*, 30, 534
- Mori, K., An, H., Burgess, D., et al. 2022, in *37th International Cosmic Ray Conference*, 963
- Mushotzky, R., Aird, J., Barger, A. J., et al. 2019, in *Bulletin of the American Astronomical Society*, Vol. 51, 107
- NASA High Energy Astrophysics Science Archive Research Center (Heasarc). 2014, *HEASoft: Unified Release of FTOOLS and XANADU*, ascl:1408.004
- Ng, C. Y., & Romani, R. W. 2004, *ApJ*, 601, 479
- Nynka, M., Hailey, C. J., Reynolds, S. P., et al. 2014, *ApJ*, 789, 72
- Park, J., Kim, C., Woo, J., et al. 2023a, *ApJ*, 945, 66
- . 2023b, *ApJ*, 945, 33
- Porter, T. A., Jóhannesson, G., & Moskalenko, I. V. 2022, *ApJS*, 262, 30
- Porth, O., Vorster, M. J., Lyutikov, M., & Engelbrecht, N. E. 2016, *MNRAS*, 460, 4135
- Reynolds, S. P. 2003, *arXiv e-prints*, arXiv:0308483
- . 2009, *ApJ*, 703, 662
- . 2016, *Journal of Plasma Physics*, 82, 635820501
- Safi-Harb, S., & Kumar, H. S. 2008, *ApJ*, 684, 532
- Sironi, L., & Cerutti, B. 2017, in *Astrophysics and Space Science Library*, Vol. 446, *Modelling Pulsar Wind Nebulae*, ed. D. F. Torres, 247
- Summerlin, E. J., & Baring, M. G. 2012, *ApJ*, 745, 63
- Tang, X., & Chevalier, R. A. 2012, *ApJ*, 752, 83
- Terrier, R., Mattana, F., Djannati-Atai, A., et al. 2008, in *American Institute of Physics Conference Series*, Vol. 1085, *American Institute of Physics Conference Series*, ed. F. A. Aharonian, W. Hofmann, & F. Rieger, 312–315
- Torres, D. F., Cillis, A., Martín, J., & de Oña Wilhelmi, E. 2014, *Journal of High Energy Astrophysics*, 1, 31
- Verner, D. A., Ferland, G. J., Korista, K. T., & Yakovlev, D. G. 1996, *ApJ*, 465, 487
- Vleschow Calas, L., Kaufmann, S., Álvarez Ochoa, C., & Tibolla, O. 2018, *Nuclear and Particle Physics Proceedings*, 297-299, 102
- Wik, D. R., Hornstrup, A., Molendi, S., et al. 2014, *ApJ*, 792, 48
- Wilms, J., Allen, A., & McCray, R. 2000, *ApJ*, 542, 914
- Woo, J., An, H., Gelfand, J. D., et al. 2023, *ApJ*, 954, 9
- Zhang, L., & Cheng, K. S. 2000, *A&A*, 363, 575
- Zhu, B.-T., Zhang, L., & Fang, J. 2018, *A&A*, 609, A110

REFERENCES

- Abeyssekara, A. U., Albert, A., Alfaro, R., et al. 2017, *Science*, 358, 911
- Adriani, O., Barbarino, G. C., Bazilevskaya, G. A., et al. 2009, *Nature*, 458, 607
- Albert, A., Alfaro, R., Alvarez, C., et al. 2020, *ApJ*, 905, 76
- Amenomori, M., Asano, S., Bao, Y. W., et al. 2023, arXiv e-prints, arXiv:2308.13781
- An, H. 2019, *ApJ*, 876, 150
- An, H., & Archibald, R. 2019, *ApJL*, 877, L10
- An, H., Madsen, K. K., Reynolds, S. P., et al. 2014a, *ApJ*, 793, 90
- An, H., Madsen, K. K., Westergaard, N. J., et al. 2014b, in *Proc. SPIE, Vol. 9144, Space Telescopes and Instrumentation 2014: Ultraviolet to Gamma Ray*, 91441Q
- Arnaud, K. A. 1996, in *Astronomical Society of the Pacific Conference Series, Vol. 101, Astronomical Data Analysis Software and Systems V*, ed. G. H. Jacoby & J. Barnes, 17
- Atwood, W. B., Abdo, A. A., Ackermann, M., et al. 2009, *ApJ*, 697, 1071
- Bamba, A., Anada, T., Dotani, T., et al. 2010a, *ApJL*, 719, L116
- . 2010b, *ApJL*, 719, L116
- Bandiera, R., Bucciantini, N., Martín, J., Olmi, B., & Torres, D. F. 2023, *MNRAS*, 520, 2451
- Bogdanov, S., Ho, W. C. G., Enoto, T., et al. 2019, *ApJ*, 877, 69
- Burgess, D. A., Mori, K., Gelfand, J. D., et al. 2022, *ApJ*, 930, 148
- Cao, Z., Aharonian, F. A., An, Q., et al. 2021, *Nature*, 594, 33
- Cao, Z., Aharonian, F., An, Q., et al. 2023, arXiv e-prints, arXiv:2305.17030
- Chen, G., An, H., Kaspi, V. M., et al. 2016, *ApJ*, 817, 93
- Chevalier, R. A. 2005, *ApJ*, 619, 839
- de Jager, O. C., & Djannati-Ataï, A. 2009, in *Astrophysics and Space Science Library, Vol. 357, Astrophysics and Space Science Library*, ed. W. Becker, 451
- de Jager, O. C., Raubenheimer, B. C., & Swanepoel, J. W. H. 1989, *A&A*, 221, 180
- Fruscione, A., McDowell, J. C., Allen, G. E., et al. 2006, in *Proc. SPIE, Vol. 6270, Society of Photo-Optical Instrumentation Engineers (SPIE) Conference Series*, 62701V
- Gabriel, C. 2017, in *The X-ray Universe 2017*, 84
- Gelfand, J. D., Slane, P. O., & Zhang, W. 2009, *ApJ*, 703, 2051
- Gotthelf, E. V., Halpern, J. P., Terrier, R., & Mattana, F. 2011, *ApJL*, 729, L16
- Guest, B. T., Safi-Harb, S., & Tang, X. 2019, *MNRAS*, 482, 1031
- H. E. S. S. Collaboration, Abdalla, H., Abramowski, A., & Aharonian, e. a. 2018, *A&A*, 612, A1
- H. E. S. S. Collaboration, Aharonian, F., Ait Benkhali, F., et al. 2023, *A&A*, 673, A148
- Harding, A. K., & Kalapotharakos, C. 2017, in *Proceedings of the 7th International Fermi Symposium*, 6
- HAWC, Abeyssekara, A. U., Albert, A., et al. 2022, in *37th International Cosmic Ray Conference*, 827
- Ho, W. C. G., Kuiper, L., Espinoza, C. M., et al. 2022, *ApJ*, 939, 7
- Kargaltsev, O., & Pavlov, G. G. 2008, in *American Institute of Physics Conference Series, Vol. 983, 40 Years of Pulsars: Millisecond Pulsars, Magnetars and More*, ed. C. Bassa, Z. Wang, A. Cumming, & V. M. Kaspi, 171–185
- Kennel, C. F., & Coroniti, F. V. 1984a, *ApJ*, 283, 694
- . 1984b, *ApJ*, 283, 710
- Kim, S., & An, H. 2020, *Astronomische Nachrichten*, 341, 170
- Kim, S., Park, J., & An, H. 2019, *Journal of Korean Astronomical Society*, 52, 173
- Kuiper, L., & Hermsen, W. 2015, *MNRAS*, 449, 3827
- Kuiper, L., Hermsen, W., & Dekker, A. 2018, *MNRAS*, 475, 1238
- LHAASO Collaboration, Cao, Z., Aharonian, F., et al. 2021, *Science*, 373, 425
- Madsen, K., Hickox, R., Bachetti, M., et al. 2019, in *Bulletin of the American Astronomical Society, Vol. 51*, 166
- Madsen, K. K., Beardmore, A. P., Forster, K., et al. 2017, *AJ*, 153, 2
- Madsen, K. K., Forster, K., Grefenstette, B., Harrison, F. A., & Miyasaka, H. 2022, *Journal of Astronomical Telescopes, Instruments, and Systems*, 8, 034003
- Madsen, K. K., Reynolds, S., Harrison, F., et al. 2015a, *ApJ*, 801, 66
- Madsen, K. K., Harrison, F. A., Markwardt, C. B., et al. 2015b, *ApJS*, 220, 8
- Manconi, S., Di Mauro, M., & Donato, F. 2020, *PhRvD*, 102, 023015
- Massaro, E., Perri, M., Giommi, P., & Nesci, R. 2004, *A&A*, 413, 489
- Molkov, S. V., Cherepashchuk, A. M., Lutovinov, A. A., et al. 2004, *Astronomy Letters*, 30, 534

- Mori, K., An, H., Burgess, D., et al. 2022, in 37th International Cosmic Ray Conference, 963
- Mushotzky, R., Aird, J., Barger, A. J., et al. 2019, in Bulletin of the American Astronomical Society, Vol. 51, 107
- NASA High Energy Astrophysics Science Archive Research Center (Heasarc). 2014, HEASoft: Unified Release of FTOOLS and XANADU, ascl:1408.004
- Ng, C. Y., & Romani, R. W. 2004, ApJ, 601, 479
- Nynka, M., Hailey, C. J., Reynolds, S. P., et al. 2014, ApJ, 789, 72
- Park, J., Kim, C., Woo, J., et al. 2023a, ApJ, 945, 66
- . 2023b, ApJ, 945, 33
- Porter, T. A., Jóhannesson, G., & Moskalenko, I. V. 2022, ApJS, 262, 30
- Porth, O., Vorster, M. J., Lyutikov, M., & Engelbrecht, N. E. 2016, MNRAS, 460, 4135
- Reynolds, S. P. 2003, arXiv e-prints, arXiv:0308483
- . 2009, ApJ, 703, 662
- . 2016, Journal of Plasma Physics, 82, 635820501
- Safi-Harb, S., & Kumar, H. S. 2008, ApJ, 684, 532
- Sironi, L., & Cerutti, B. 2017, in Astrophysics and Space Science Library, Vol. 446, Modelling Pulsar Wind Nebulae, ed. D. F. Torres, 247
- Summerlin, E. J., & Baring, M. G. 2012, ApJ, 745, 63
- Tang, X., & Chevalier, R. A. 2012, ApJ, 752, 83
- Terrier, R., Mattana, F., Djannati-Atai, A., et al. 2008, in American Institute of Physics Conference Series, Vol. 1085, American Institute of Physics Conference Series, ed. F. A. Aharonian, W. Hofmann, & F. Rieger, 312–315
- Torres, D. F., Cillis, A., Martín, J., & de Oña Wilhelmi, E. 2014, Journal of High Energy Astrophysics, 1, 31
- Verner, D. A., Ferland, G. J., Korista, K. T., & Yakovlev, D. G. 1996, ApJ, 465, 487
- Vleeschower Calas, L., Kaufmann, S., Álvarez Ochoa, C., & Tibolla, O. 2018, Nuclear and Particle Physics Proceedings, 297-299, 102
- Wik, D. R., Hornstrup, A., Molendi, S., et al. 2014, ApJ, 792, 48
- Wilms, J., Allen, A., & McCray, R. 2000, ApJ, 542, 914
- Woo, J., An, H., Gelfand, J. D., et al. 2023, ApJ, 954, 9
- Zhang, L., & Cheng, K. S. 2000, A&A, 363, 575
- Zhu, B.-T., Zhang, L., & Fang, J. 2018, A&A, 609, A110

This figure "orcid-ID.png" is available in "png" format from:

<http://arxiv.org/ps/2311.12376v1>